POD-Based Characterization of KH-Driven Surface Waves and Hierarchical Breakup Structures in a Liquid Jet in Crossflow

Yingming Si[1,*], Tianyi Wang[1], Yannis Hardalupas[1]

1: Dept. of Mechanical Engineering, Imperial College London, United Kingdom
* Correspondent author: ys2624@ic.ac.uk

Keywords: Liquid jet in crossflow, Modal analysis, Proper orthogonal decomposition, Kelvin-Helmholtz instability, Breakup regimes

ABSTRACT

The near-field atomization of a liquid jet in crossflow (LJIC) is investigated experimentally using high-speed shadowgraphy across four breakup regimes, including the column, bag, multimode, and shear breakup regimes, with gaseous Weber numbers ranging from We_g = 2.5 to 249.5 and liquid-to-gas momentum ratio from M = 1.0 to 222.7. Proper orthogonal decomposition (POD) combined with Welch spectral analysis and phase averaging is applied to time-resolved image sequences to extract dominant spatial and temporal structures. A dedicated cropped-window analysis on the windward pre-breakup region is introduced to isolate surface-wave modes otherwise obscured by the energetically dominant post-breakup structures in full-field decompositions.

Two physically distinct dominant structures are identified across operating conditions: a pre-breakup surface-wave mode exhibiting streamwise-periodic undulations on the windward liquid surface, and a post-breakup structural mode associated with the periodic formation and downstream convection of breakup products including bags, ligaments, and droplet clusters. The wavelength of surface-wave mode decreases and frequency increases monotonically with We_g in the column and early bag-breakup regimes, consistent with increasing aerodynamic forcing at higher crossflow velocities. The wavelength on the post-breakup structural mode reaches a local minimum near the bag-to-multimode transition. Within the bag-breakup regime, cases where both modes are simultaneously extractable exhibit wavelength ratios and frequency ratios that remain approximately constant within each liquid-jet velocity group, alongside near-unity propagation speed ratios with both speeds close to the liquid-jet velocity. These results suggest that breakup structures emerge as nonlinear secondary structures periodically selected from a precursor interfacial wave train, with a clear hierarchical nesting relationship between the two.

In the column and bag-breakup regime, the wavelengths of the surface-wave modes agree in magnitude with the most-unstable wavelengths predicted by the classical Kelvin–Helmholtz (KH) instability theory. Meanwhile, the theoretical propagation speeds of these waves are close to the liquid-jet velocity, which confirms a convective KH mechanism governing pre-breakup interfacial-wave selection. In general, the four breakup regimes can be interpreted as reflecting the competition between KH-driven interfacial-wave growth and direct aerodynamic shear stripping: KH waves dominate in the column and bag regimes, both mechanisms coexist in the multimode regime, and shear stripping prevails in the shear regime.

1. Introduction

Liquid jets in crossflow (LJIC) are relevant to a broad range of engineering applications, including fuel injection in gas-turbine combustors, thrust-vector control, and film cooling (Wu et al., 1997; Mahesh, 2013; Lefebvre & McDonell, 2017). When a liquid jet is injected transversely into a gas stream, it undergoes column bending, surface waviness, primary breakup, and droplet formation driven by aerodynamic forcing, which directly govern downstream mixing, evaporation, and combustion performance (Lin, 2003; Zhou et al., 2023; Shaw et al., 2024).

The breakup behavior of LJIC has been systematically characterised through experimental studies. Wu et al. identified the column, bag, multimode, and shear breakup regimes, governed primarily by the gaseous Weber number, We_g (Wu et al., 1997), while Sallam et al. provided detailed shadowgraphic observations of the corresponding surface structures (Sallam et al., 2002, 2004). Ng et al. further enriched the phenomenological understanding of bag formation and evolution (Ng et al., 2008). Through these efforts, a relatively mature breakup-regime framework has been established, although the boundaries between regimes may vary slightly depending on We_g.

From a physical standpoint, LJIC breakup is conventionally attributed to the coupling of Rayleigh-Taylor (RT) and Kelvin-Helmholtz (KH) instabilities, associated respectively with crossflow-induced normal acceleration and interfacial shear (Sallam et al., 2004; Zhou et al., 2023). However, recent experimental and numerical studies have increasingly pointed towards a KH-dominated mechanism for near-field surface-wave generation. Bhatia et al. showed through high-fidelity VOF simulations that surface waves in the column and bag regimes are more consistently described by KH scaling than by RT instability (Bhatia et al., 2023). Shaw et al. reached a similar conclusion from high-resolution shadowgraphy, reporting that measured surface-wave wavelengths and propagation speeds are more consistent with KH predictions, particularly at moderate Weber numbers (Shaw et al., 2024). Medipati et al. further demonstrated that geometric effects can alter the relative contributions of RT and KH instabilities (Medipati et al., 2025). Despite this progress, a quantitative mapping of KH instability onto experimentally observable interfacial structures — spanning wavelength, frequency, and propagation speed across multiple breakup regimes — remains lacking.

On the diagnostic side, shadowgraphy remains the primary tool for capturing column trajectories and global breakup morphology, while advanced techniques such as digital holography, particle image velocimetry, planar laser-induced fluorescence, and optical connectivity have enabled more detailed characterization of local velocity fields, droplet sizes, and interfacial geometry (Charalampous et al., 2016; Johnson et al., 2024; Shaw et al., 2024). Modal-analysis methods, particularly POD, have recently been applied to atomization problems to extract dominant coherent structures from time-resolved image data (Charalampous et al., 2019; Soni &

Kolhe, 2021; Harikumar et al., 2025), but have not yet been systematically applied to LJIC. Furthermore, under pronounced breakup conditions, pre-breakup surface waves are energetically obscured by stronger post-breakup fluctuations, like ligaments, bag structures, and dense droplet clouds, making their systematic extraction and quantification across operating conditions difficult.

The present study aims to address these gaps by applying Proper Orthogonal Decomposition (POD), combined with Welch spectral analysis and phase averaging, to high-speed shadowgraphy images of an LJIC under operating conditions across the column, bag, multimode and shear breakup regime. A dedicated cropped-window analysis is introduced to isolate pre-breakup surface-wave modes from energetically dominant post-breakup structures. The analysis seeks to quantify the dominant spatial and temporal characteristics of near-field structures as functions of We_g, examine the hierarchical relationship between pre-breakup surface waves and post-breakup breakup structures, and assess the consistency of quantified wavelengths and propagation speeds with KH instability theory. The remainder of this paper is organised as follows. Section 2 describes the experimental setup and analysis methodology; Section 3 presents the results; Section 4 provides physical interpretation and discussion; and Section 5 summarises the conclusions.

2. Methodology

2.1. Experimental set-up and operating conditions

Experiments were conducted using a vertically arranged gas-crossflow atomizer; full details of the facility are given in our previous work (Wang & Hardalupas, 2023, 2025). Briefly, compressed air entered a plenum, passed through a flow-conditioning section, and was accelerated through a contraction into a transparent glass test section, establishing a nearly uniform crossflow. Deionised water was injected normally into the crossflow through a circular orifice of diameter D = 1 mm on the side wall. High-speed shadowgraphy was employed to resolve liquid-interface structures and breakup dynamics. An LED backlight, synchronised with the camera, provided high-contrast silhouette images acquired at 6000 fps with a resolution of 1024×516 pixels, covering a physical field of view of 26.5 mm×13.3 mm (spatial resolution ≈ 25.9 μm/pixel).

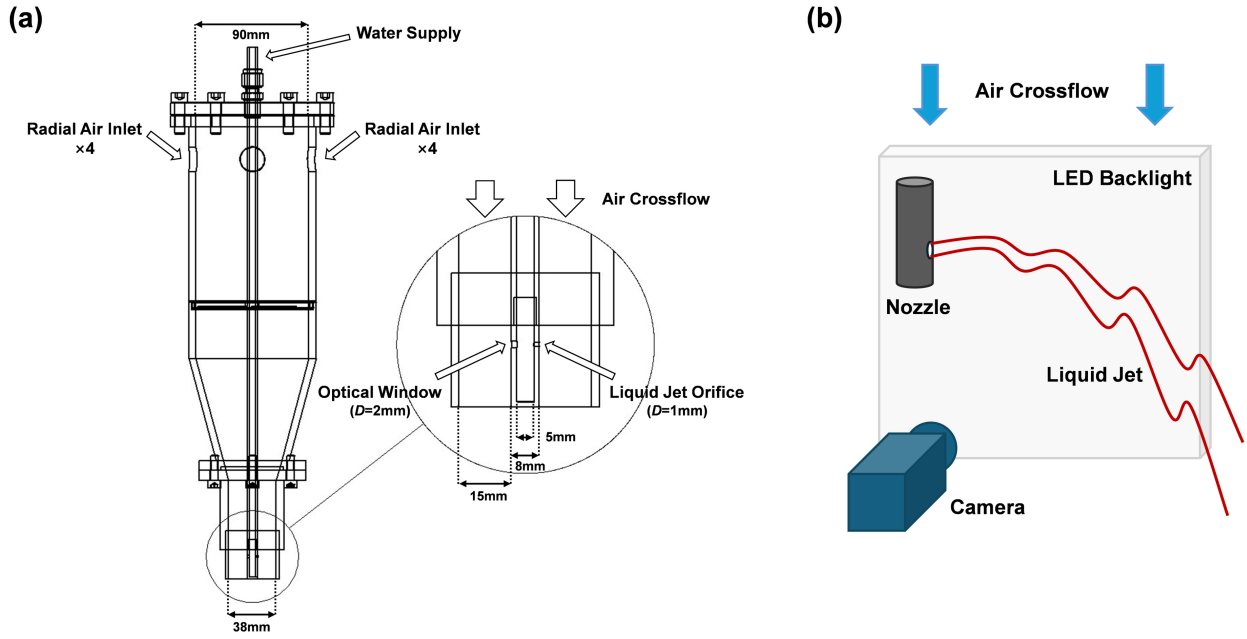


Figure 1. Gas crossflow atomizer structure (a) and experimental setup schematic (b)

Deionised water and compressed air were used as the liquid and gas phases, respectively, with physical properties listed in Table 1.

Table 1. Physical properties of the working fluids

$\rho_l(kg/m^3)$	$\rho_g(kg/m^3)$	$\mu_l(pa \cdot s)$	$\mu_g(pa \cdot s)$	$\gamma(N/m)$
998	1.2	0.001	1.8×10^{-5}	0.0728

The flow is characterized by the gaseous Weber number, We_g, and liquid-to-gas momentum ratio, M, defined respectively as:

$$We_g = \frac{\rho_g U_g^2 D}{\gamma} \quad (1)$$

$$M = \frac{\rho_l U_l^2}{\rho_g U_g^2} \quad (2)$$

where ρ_l, ρ_g are the liquid and gas densities, U_l, U_g the respective jet and crossflow velocities, and γ the surface tension. Crossflow and liquid-jet velocities were varied to span all four breakup regimes, yielding 32 operating conditions across two liquid-jet velocities and sixteen crossflow velocities, as listed in Table 2. In each group, the liquid velocity, U_l, is kept constant, while We_g and M vary with the changing crossflow velocity, U_g. Breakup-regime boundaries used in current study follow the criterion of Sallam et al., with transitions at We_g = 4, 30, and 110 (Sallam et al., 2004).

Table 2. LJIC operating conditions

Group	Case	$U_l(m/s)$	$U_g(m/s)$	We_g	M	Breakup Regime
A	1	4.2	12.3	2.5	99.0	Column

	2		13.8	3.2	78.2	Column
	3		15.4	3.9	63.4	Column
	4		16.9	4.7	52.4	Bag
	5		18.5	5.6	44.0	Bag
	6		20.0	6.6	37.5	Bag
	7		24.6	10.0	24.7	Bag
	8		30.7	15.6	15.8	Bag
	9		38.4	24.4	10.1	Bag
	10		43.1	30.6	8.1	Multimode
	11		49.2	40.0	6.2	Multimode
	12		61.5	62.4	4.0	Multimode
	13		73.8	90.0	2.7	Multimode
	14		89.2	131.1	1.9	Shear
	15		98.4	160.0	1.5	Shear
	16		123.0	249.5	1.0	Shear
B	1	6.4	12.3	2.5	222.7	Column
	2		13.8	3.2	176.0	Column
	3		15.4	3.9	142.5	Column
	4		16.9	4.7	117.8	Bag
	5		18.5	5.6	99.0	Bag
	6		20.0	6.6	84.3	Bag
	7		24.6	10.0	55.7	Bag
	8		30.7	15.6	35.6	Bag
	9		38.4	24.4	22.8	Bag
	10		43.1	30.6	18.2	Multimode
	11		49.2	40.0	13.9	Multimode
	12		61.5	62.4	8.9	Multimode
	13		73.8	90.0	6.2	Multimode
	14		89.2	131.1	4.2	Shear
	15		98.4	160.0	3.5	Shear
	16		123.0	249.5	2.2	Shear

2.2 Image analysis framework

For each operating condition, 4096 consecutive shadowgraph frames were acquired. Raw frames were converted to grayscale and the temporal mean was subtracted to form a fluctuation

matrix, on which all subsequent analyses were performed. In addition to the full-field analysis, a secondary cropped window focusing on the windward pre-breakup interface was defined for each case to reduce interference from downstream droplet clouds and post-breakup structures.

POD was applied to the fluctuation matrix to extract energetically dominant coherent structures (Lumley, 1967; Sirovich, 1987; Berkooz et al., 1993). Because POD ranks modes by energy, low-order modes of full-field images preferentially capture post-breakup structures, like bags, ligaments, and droplet clouds, whose grayscale fluctuations are considerably stronger than those of pre-breakup surface waves. Restricting the decomposition to the cropped pre-breakup window suppresses this masking effect and allows surface-wave modes to emerge at low order. Both full-field and cropped-window decompositions were performed for each operating condition.

The power spectral density of each POD temporal coefficient was estimated using the Welch method (Welch, 1967) to identify dominant periodic modes. Spatial modes displaying a distinct narrowband spectral peak were retained as candidates for wavelength and frequency extraction. Characteristic wavelength was estimated from the candidate spatial modes as the mean distance between adjacent zero-crossings along the principal propagation direction. The dominant frequency was taken as the Welch peak frequency of the corresponding temporal coefficient.

For mode pairs with similar frequencies, comparable energies, and approximately quadrature spatial structures, phase averaging was applied to reconstruct the repeatable periodic fluctuation field over one mean cycle, providing direct visual verification of the physical periodicity identified spectrally.

For each periodic mode, the modal propagation speed was then defined as:

$$c = f\lambda \tag{3}$$

This quantity represents the theoretical convective speed of the dominant structures: the propagation speed of interfacial instability waves before breakup, or the convective speed of post-breakup structures after breakup. The extracted λ, f, and c are plotted against We_g alongside breakup-regime boundaries to examine how dominant structural scales and dynamics evolve across regimes.

3. Results

3.1 Representative experimental images

Figure 2 shows representative shadowgraphic images at We_g = 2.5, 10, 40, and 160 for both liquid-jet velocity groups, which fall into the column, bag, multimode and shear breakup regimes, respectively. With increasing crossflow velocity, the liquid column transitions from a nearly intact continuous form to configurations exhibiting pronounced surface undulations, bag-like bulging, ligaments, and dense droplet clouds. Besides, increasing liquid-jet velocity increases penetration

depth and shifts the breakup location downstream. The image sequences thus contain multi-scale spatial-temporal information spanning global column motion, interfacial-wave dynamics, and post-breakup structures, motivating the modal decomposition approach described in Section 2.

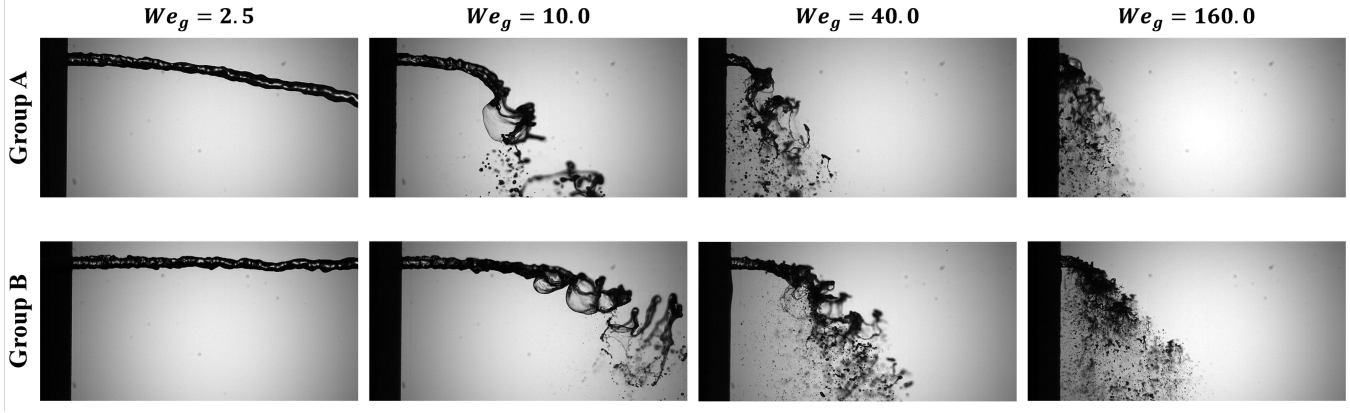


Figure 2. LJIC images under typical operating conditions.

3.2 Identification of dominant structure types

Three classes of dominant structures are identified across operating conditions, as illustrated in Figure 3: (a) a global liquid-column flapping mode — low-frequency, large-scale transverse motion of the entire liquid column; (b) a pre-breakup surface-wave mode — streamwise-periodic undulations on the windward liquid-column surface upstream of the breakup point; and (c) a post-breakup structural mode — periodic recurrence of breakup products including bags, ligaments, or droplet clusters in the downstream region. This classification is consistent with prior observations (Arienti & Soteriou, 2009; Leask & McDonell, 2019; Wang & Hardalupas, 2025). The POD analysis results of the experimental images identified modes with corresponding characteristics at the corresponding locations.

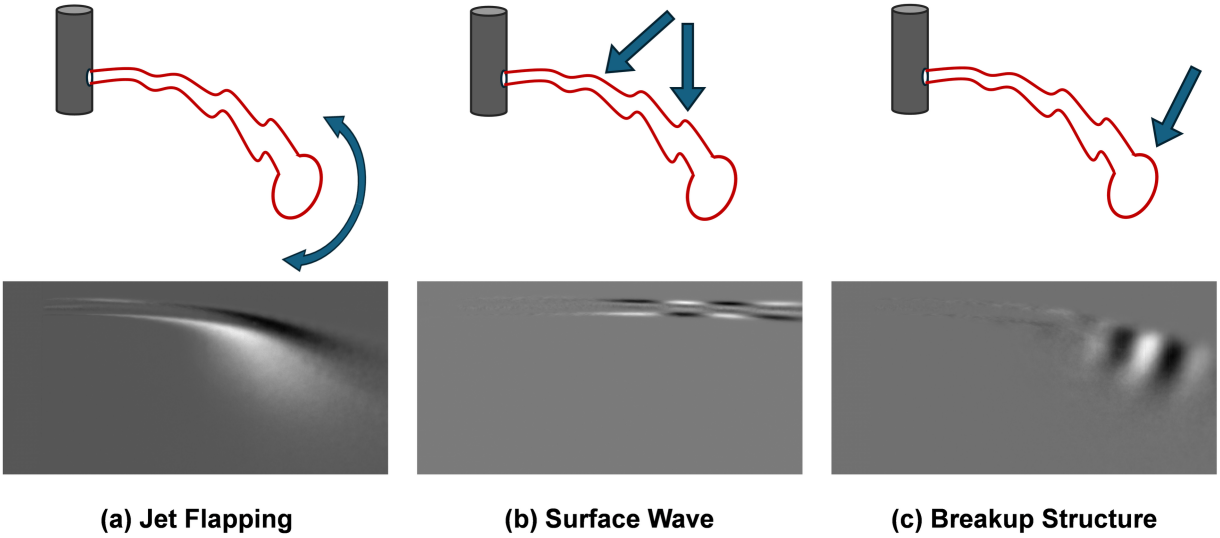


Figure 3. The dominant structures in LJIC. (a) global liquid-column flapping mode; (b) pre-breakup surface-wave mode; (c) post-breakup structural mode. The POD modal images were selected from different cases.

Because POD ranks modes by energy, the relative prominence of these structure types in the decomposition depends on operating conditions. Pre-breakup surface waves dominate the low-order modes when no prominent breakup structures are present. Once bags or ligaments form, their stronger grayscale fluctuations dominate the low-order modes, displacing surface-wave modes to higher order. The following subsection demonstrates how full-field and cropped-window analyses of images are combined to reliably extract both structure types.

3.3. POD modal analysis: method demonstration on case B-7 of Table 2

Case B-7 of Table 2 ($We_g = 10$, bag-breakup regime) is used as a representative example to demonstrate the extraction procedure, as it lies within the bag-breakup regime where both surface-wave and post-breakup structural modes are simultaneously present.

Full-field decomposition. Figure 4 shows the modal energy spectrum and cumulative energy distribution for case B-7. The first 241 modes account for approximately 60% of the total energy, and reconstructions using these modes recover the principal liquid-column contour and breakup structures with good fidelity (Figure 3c). The first six spatial modes are shown in Figure5. Modes 1 and 3 exhibit vertically stratified patterns dominated by transverse variation, indicating association with global liquid-column flapping. Modes 4 and 5 display a regular streamwise-periodic distribution concentrated in the post-breakup region; their near-identical spatial shapes identify them as a mode pair representing the same periodic breakup structure at different phases, with characteristic wavelength $\lambda_{str} \approx 3.5$ mm. Welch spectral analysis of the temporal coefficients (Figure 6) confirms this interpretation: modes 1, 2, 3, and 6 exhibit dominant peaks at frequencies below 500 Hz consistent with global flapping, while modes 4 and 5 share a dominant peak at frequency $f_{str} \approx 1850$ Hz corresponding to the observed bag-formation period.

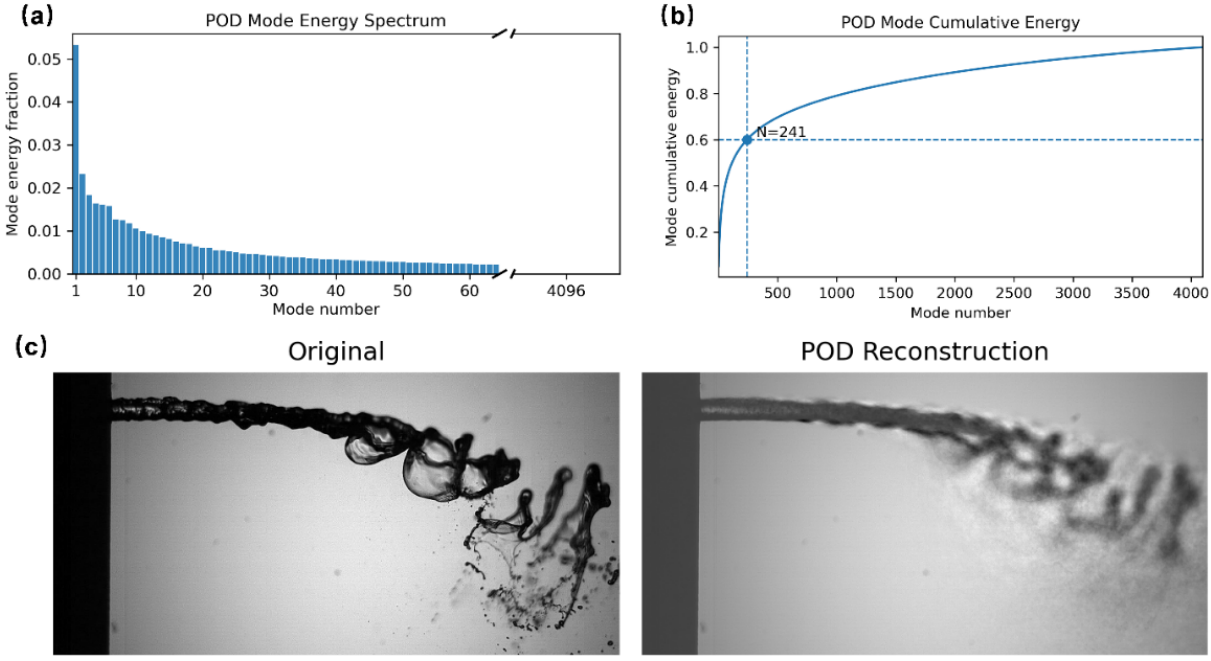


Figure 4. POD modal energy distribution (a), cumulative POD modal energy distribution (b), and comparison of the reconstructed image with the original image (c) for Case B-7 of Table 2.

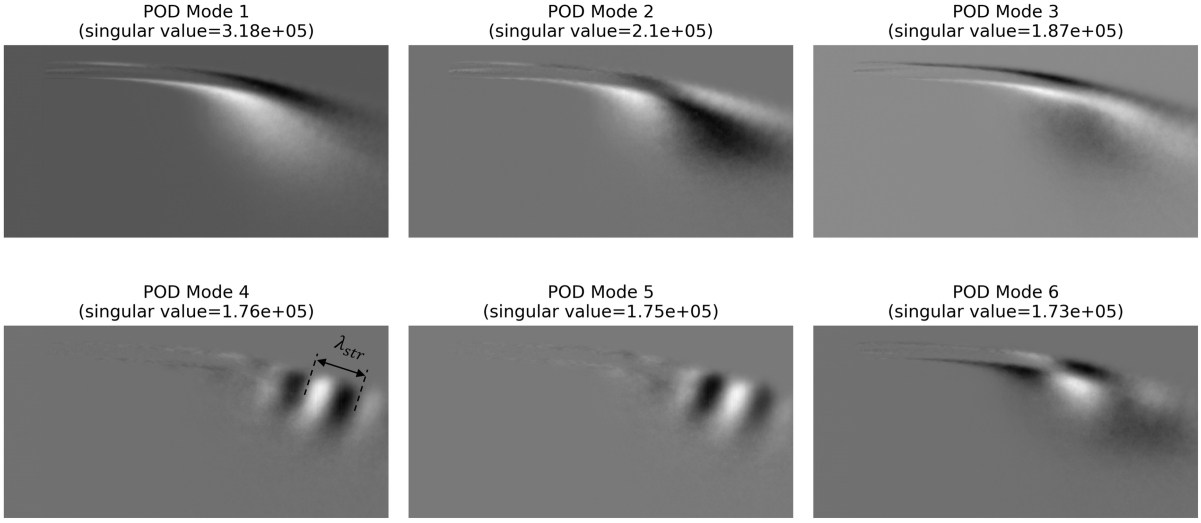


Figure 5. The first six POD mode shapes of Case B-7 of Table 2.

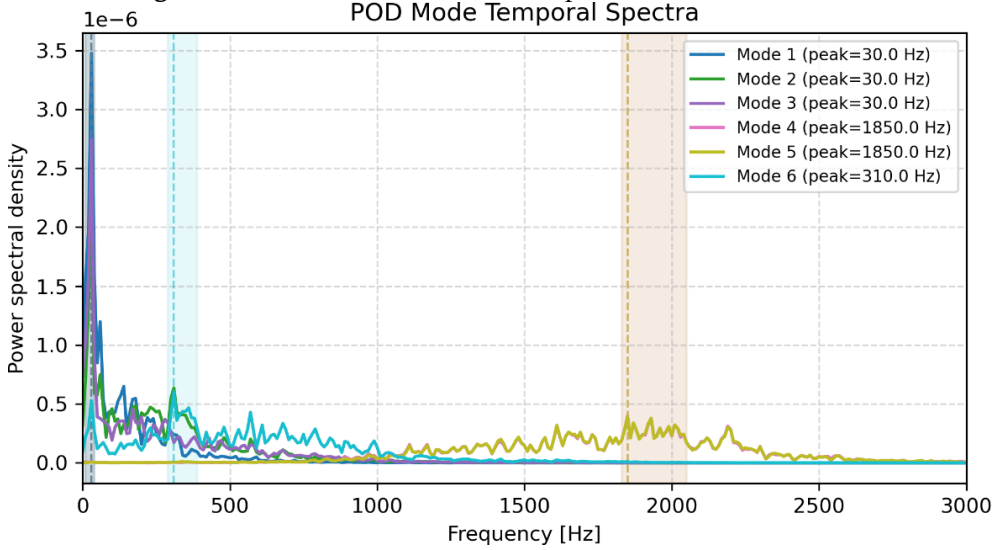


Figure 6. Power spectral densities of the first six POD modes of Case B-7 of Table 2

Cropped-window decomposition. Under bag-breakup conditions, post-breakup structures dominate the low-order full-field modes, masking the weaker pre-breakup surface waves. Repeating the POD and Welch analyses on a cropped window upstream of the breakup point (Figure 7) allows surface-wave modes to emerge at low order. Mode 6 of this decomposition exhibits a clear interfacial-wave spatial structure (Figure 8), yielding a characteristic wavelength $\lambda_{\text{wave}} \approx 2.2$ mm and frequency $f_{\text{wave}} = 2840$ Hz (Figure 9). This confirms that pre-breakup surface waves persist under breakup conditions, but are energetically masked in the full-field decomposition.

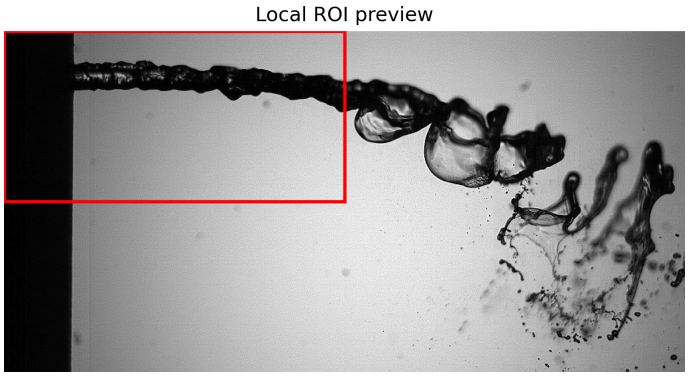


Figure 7. The sampling range of the pre-breakup window of Case B-7 of Table 2

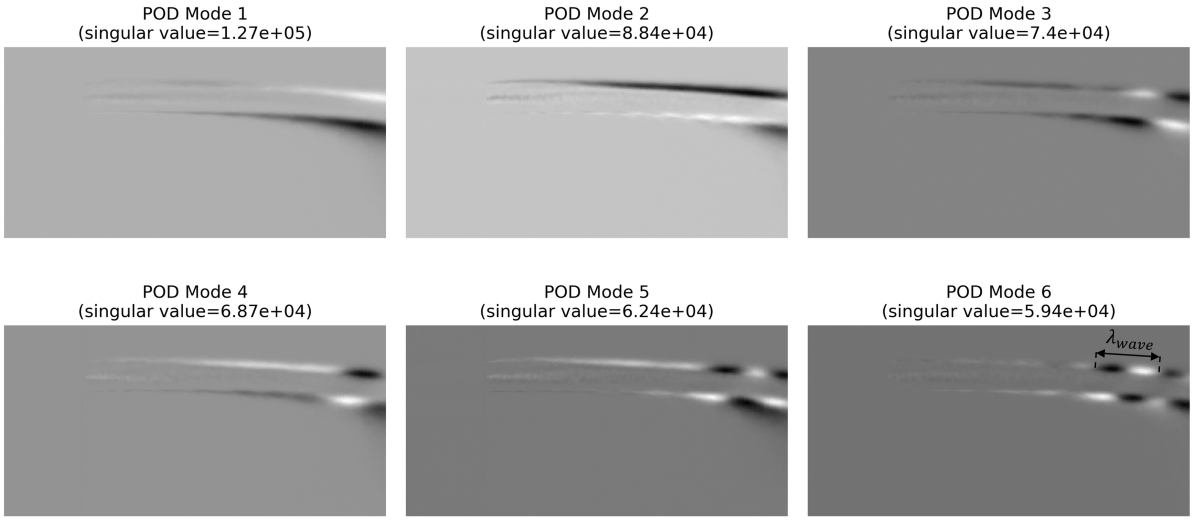


Figure 8. The first six POD mode shapes in the pre-breakup window of Case B-7 of Table 2.

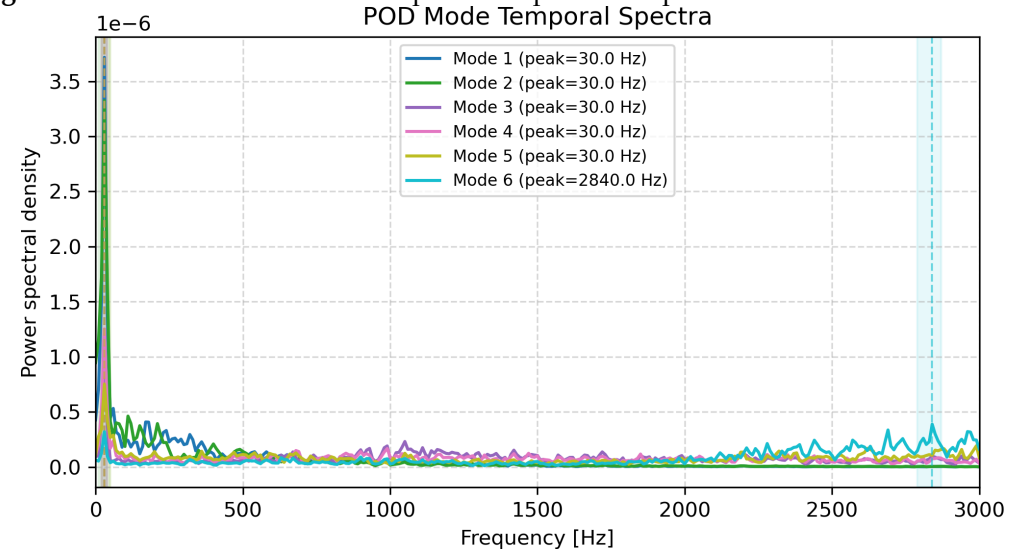


Figure 9. Power spectral densities of the first six POD modes in the pre-breakup window for Case B-7 of Table 2

Phase averaging. Phase averaging was performed using modes 4 and 5 (Figure 5) as the phase-locking pair. The resulting phase-averaged images and fluctuation fields (Figure 10) reveal a stable, repeatable structure whose location corresponds closely to the breakup region in the

raw images, independently validating the physical periodicity identified by the Welch peak frequency.

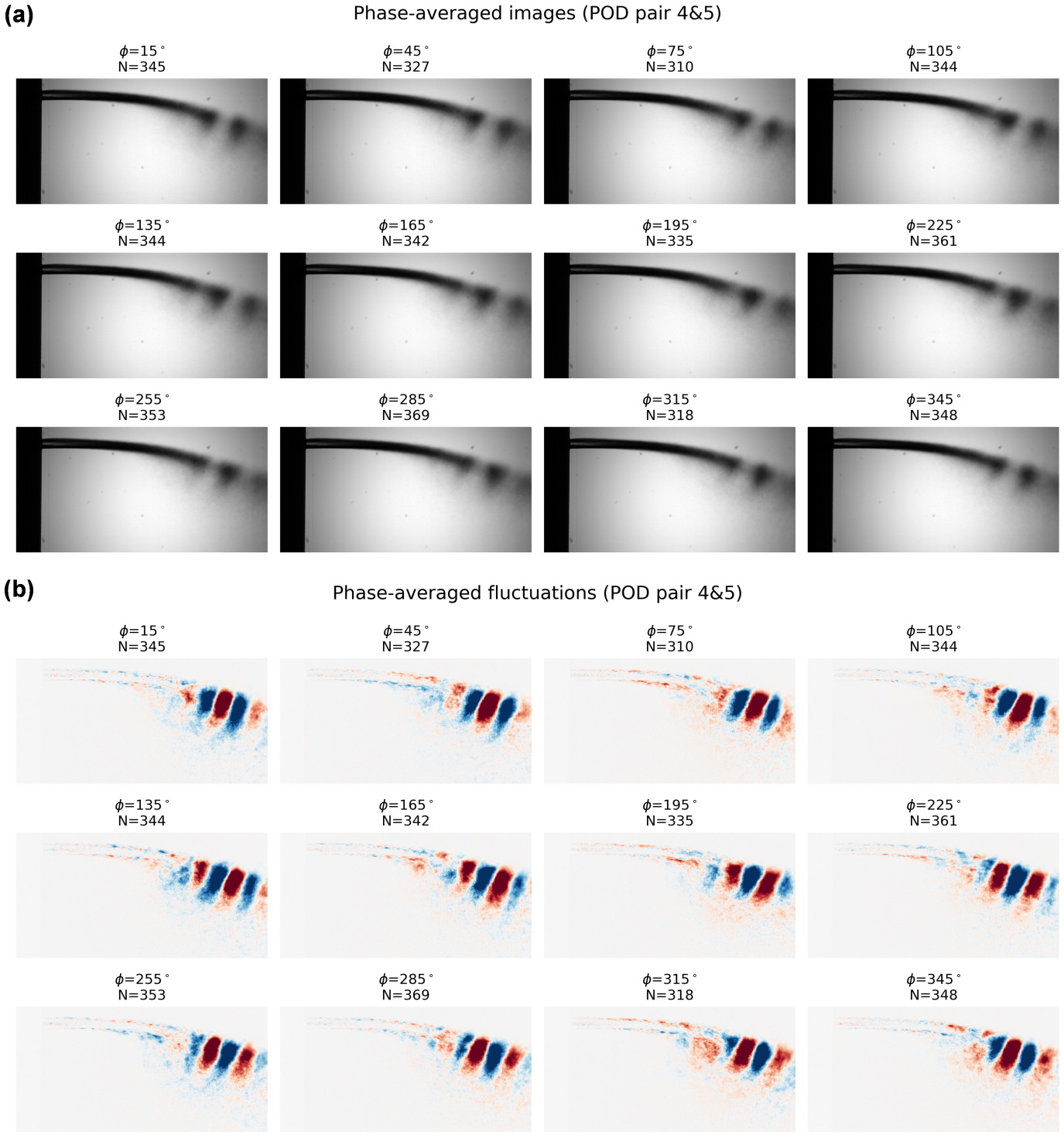


Figure 10. Phase-average images (a) and fluctuation fields (b) of Case B-7 of Table 2 with mode 4 and 5 phase-locked

3.4. Variation of wavelength, frequency and propagation speed with Weber number

Characteristic wavelengths of both dominant structure types were extracted for all cases. Results for Groups A and B are shown in Figure 11, where orange curves denote surface-wave wavelength λ_{wave} and blue curves denote post-breakup structure wavelength λ_{str}; dashed lines

mark breakup-regime boundaries. In both groups, λ_{wave} decreases monotonically with increasing We_g for $We_g < 16$, reflecting the selection of shorter instability wavelengths under stronger aerodynamic forcing. The post-breakup structure wavelength λ_{str} decreases over $10 < We_g < 30$, reaches a local minimum near the bag-to-multimode transition, and then increases for $We_g > 30$.

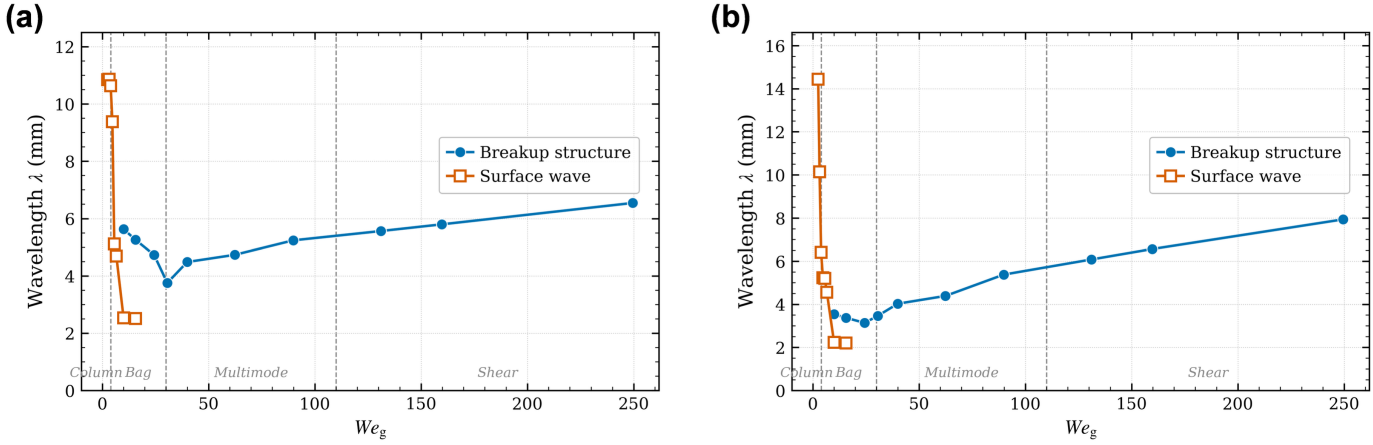


Figure 11. Variation of surface wave and breakup structure wavelengths with We for cases of Groups A and B of Table 2.

Dominant-mode frequencies are shown for cases of Groups A and B of Table 2 in Figure 12. In both groups, f_{wave} increases with We_g for $We_g < 16$, consistent with the monotonic decrease in λ_{wave} under increasing aerodynamic forcing. The post-breakup structure frequency f_{str} increases overall for $We_g > 10$.

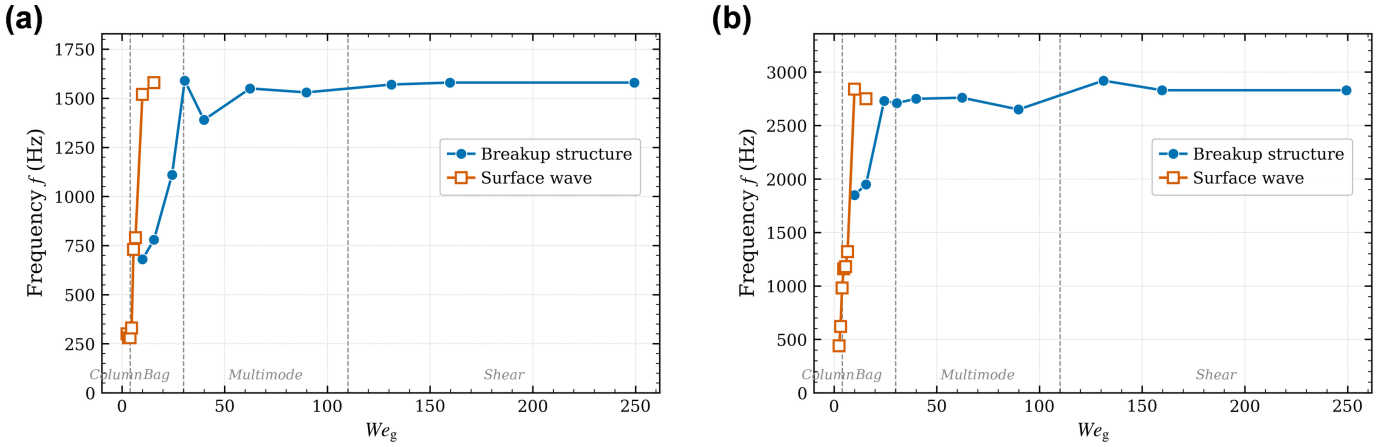


Figure 12. Variation of surface wave and breakup structure frequencies with We for cases of Groups A and B of Table 2.

Modal propagation speeds are shown for cases of Groups A and B of Table 2 in Figure 13. For the surface-wave mode, c_{wave} gradually approaches the liquid-jet velocity U_l of each group (≈ 4 m/s for Group A; ≈ 6.2 m/s for Group B) for $We_g < 16$. The post-breakup structure propagation speed c_{str} remains comparable to c_{wave} within the early bag-breakup regime, but progressively exceeds the liquid-jet velocity as We_g increases into the multimode and shear regimes.

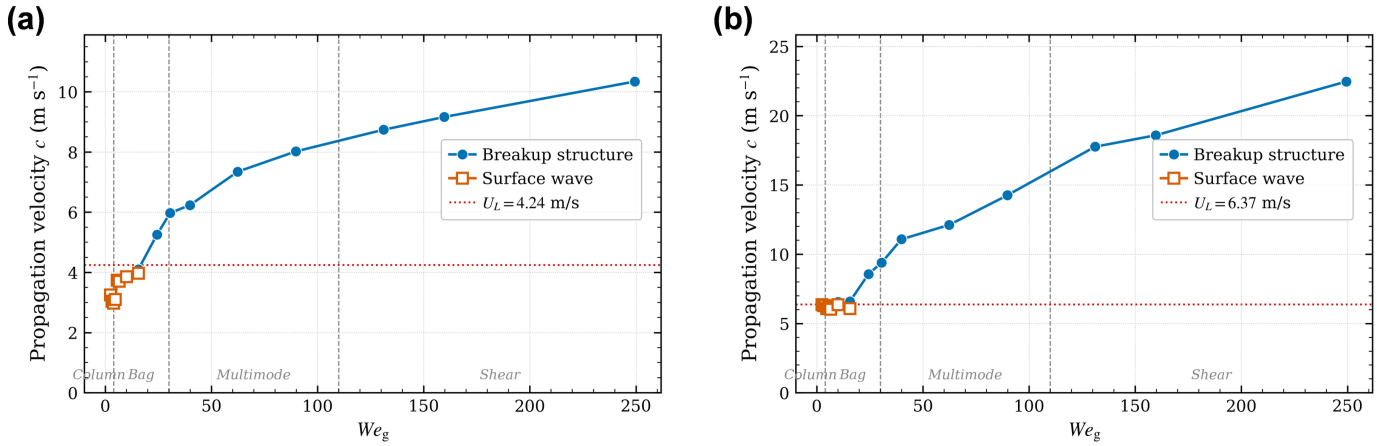


Figure 13. Variation of surface wave and breakup structure propagation speeds with We for cases of Groups A and B of Tabke 2.

For cases where both surface wave and breakup structure are simultaneously measurable (A-7, A-8, B-7, B-8), the wavelength ratio $\lambda_{str}/\lambda_{wave}$ and frequency ratio f_{wave}/f_{str} remain approximately constant within each liquid-jet velocity group, and the propagation speed ratio c_{wave}/c_{str} is close to unity, as listed in Table 3.

Table 3. Wavelength, frequency and propagation speed ratios of the surface wave and breakup structure for cases where both are simultaneously measurable

Case	$\lambda_{str}/\lambda_{wave}$	f_{wave}/f_{str}	c_{wave}/c_{str}
A-7	2.22	2.24	1.01
A-8	2.09	2.03	0.97
B-7	1.58	1.54	0.97
B-8	1.53	1.41	0.92

4. Discussion

4.1. Consistency with Kelvin–Helmholtz (KH) instability

The pre-breakup surface waves identified in Section 3 exhibit three characteristics that are more consistent with a KH mechanism than with RT instability (Chandrasekhar, 1981; Drazin & Reid, 2004). First, these waves are streamwise-periodic and confined to the windward liquid-column surface, where the shear force between the airflow and the liquid begins to dominate, rather than distributed around the column circumference as would be expected for RT-driven normal-acceleration instability. Second, the measured propagation speeds c_{wave} approach the liquid-jet velocity U_l in both groups, indicating that the waves are convected primarily by the liquid column rather than driven by crossflow-induced body forces. Third, the monotonic decrease of λ_{wave} with We_g is qualitatively consistent with KH scaling, in which stronger aerodynamic shear selects shorter instability wavelengths.

To assess consistency with KH scaling, the classical two-layer inviscid dispersion relation is used as a theoretical reference (Michalke, 1964; Chandrasekhar, 1981):

$$\omega = k\frac{\rho_g U_g+\rho_l U_l}{\rho_g+\rho_l} \pm \sqrt{\frac{\gamma k^3}{\rho_g+\rho_l} - \frac{\rho_g\rho_l}{(\rho_g+\rho_l)^2}(U_g-U_l)^2k^2} \quad (4)$$

Instability occurs for wavenumbers $0 < k < k_c$, where the critical and most unstable wavenumbers are:

$$k_m = \frac{2}{3}\frac{\rho_g\rho_l}{\gamma(\rho_g+\rho_l)}(U_g-U_l)^2 \quad (5)$$

giving the most unstable wavelength:

$$\lambda_m = 2\pi/k_m \quad (6)$$

Theoretical predictions of λ_m, computed assuming the air crossflow and liquid jet velocities remain approximately constant and parallel before breakup, are compared with experimentally measured surface-wave wavelengths in Figure 14. The two agree well in order of magnitude and exhibit broadly similar trends with We_g across the column and bag-breakup regimes. Given that the model neglects interfacial curvature, finite shear-layer thickness, viscosity, and three-dimensional crossflow effects, this level of agreement strongly suggests that the dominant pre-breakup wave train reflects the instability scale selected by the competition between local gas-liquid shear and surface tension, rather than unorganised random fluctuation. The measured propagation speeds close to U_l further confirm a convective KH mechanism, in which the gas-liquid velocity difference governs wave selection while downstream propagation is controlled by liquid-column convection. These findings are consistent with recent experimental and numerical evidence pointing towards KH-dominated near-field surface-wave generation in LJICs (Bhatia et al., 2023; Shaw et al., 2024; Wang & Hardalupas, 2025).

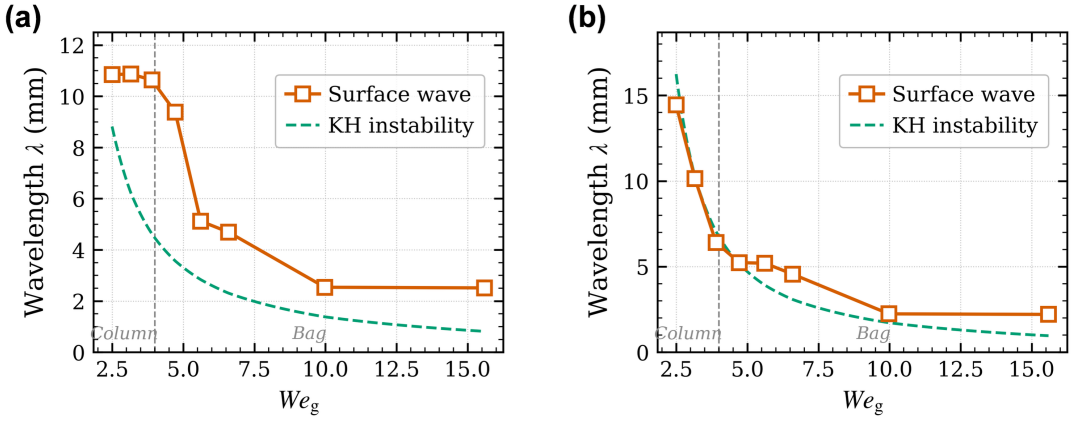


Figure 14. Comparison of the theoretically critical wavelengths of the KH instability and the experimentally measured surface wave wavelengths for cases of the three groups of Table 2.

4.2. Hierarchical relationship between surface waves and post-breakup structures

Within the bag-breakup regime, the ability to extract simultaneously both surface-wave and post-breakup structural modes for cases A-7, A-8, B-7, and B-8 of Table 2 provides an opportunity

to examine their dynamical relationship. Three observations from Section 3 are relevant. First, the wavelength ratio $\lambda_{\mathrm{str}}/\lambda_{\mathrm{wave}}$ and frequency ratio $f_{\mathrm{wave}}/f_{\mathrm{str}}$ remain approximately constant within each liquid-jet velocity group, indicating that the two structure types maintain a fixed scale relationship tied to the jet velocity rather than varying independently with We_g. Second, the propagation speed ratio $c_{\mathrm{wave}}/c_{\mathrm{str}}$ is close to unity, with both speeds approaching the liquid-jet velocity U_l, confirming that both structure types are convected primarily by the liquid column. Third, the post-breakup structure frequency f_{str} is lower than the surface-wave frequency f_{wave}, meaning breakup structures appear less frequently than the precursor waves that precede them.

These three observations together support a hierarchical nesting interpretation: a regular KH-driven surface-wave train first develops on the windward side of the liquid column and propagates downstream at approximately the liquid-jet velocity; as waves amplify nonlinearly, only those crests where local thickness, curvature, and aerodynamic forcing jointly exceed a threshold develop into fully formed breakup structures. The resulting bags therefore appear at lower frequency and larger spacing than the precursor waves, with the scale ratio remaining approximately fixed within each jet-velocity group because both processes are governed by the same convective speed. The post-breakup structures are thus more appropriately interpreted as nonlinear secondary structures periodically selected from a precursor KH wave train, rather than as independently driven dynamical processes.

It is noted that this hierarchical interpretation is inferred from a limited subset of cases within the bag-breakup regime where both modes are simultaneously extractable. Whether analogous relationships persist in the multimode or shear regimes, where direct aerodynamic stripping becomes increasingly dominant and pre-breakup surface waves are more difficult to isolate, remains an open question for future work.

4.3. Overall picture of the breakup mechanism

The results of Section 3 and the interpretations of Sections 4.1–4.2 together suggest an overall picture of near-field LJIC atomization governed by two concurrent processes: (1) a KH-driven interfacial-wave process along the windward liquid-column surface, generating a convective wave train that develops nonlinearly into periodic breakup structures; and (2) direct aerodynamic stripping from the column surface by the crossflow, promoting continuous ligament and droplet shedding independent of the wave-growth process.

The four breakup regimes reflect the competition between these two processes as We_g increases. In the column regime, KH surface waves are present and measurable but remain below the threshold for bag formation; the column breaks up primarily through tip stripping and column fracture driven by aerodynamic drag. In the bag regime, a subset of surface-wave crests exceeds the bag-formation threshold, and periodic bag-like structures detach from the column, giving rise

to the hierarchical structure documented in Section 4.2; direct stripping is present but secondary. In the multimode regime, both bag formation and direct stripping occur simultaneously at comparable intensities, reflected in the local minimum of λ_{str} near the bag-to-multimode transition and the increasing post-breakup structure propagation speed beyond the liquid-jet velocity. In the shear regime, strong aerodynamic stripping suppresses organized bag formation entirely, and the dominant structures shift to ligaments and droplets shed continuously from the column surface.

This picture is consistent with prior phenomenological descriptions of LJIC breakup (Wu et al., 1997; Sallam et al., 2004; Ng et al., 2008) while providing a quantitative mechanistic basis grounded in KH instability theory and supported by the modal analysis results of Section 3.

5. Conclusions

High-speed shadowgraphy combined with POD, Welch spectral analysis, and phase averaging was applied to LJIC near-field atomization across 32 operating conditions spanning four breakup regimes. The main conclusions are as follows.

1. A dedicated cropped-window POD analysis of the windward pre-breakup region successfully isolated pre-breakup surface-wave modes otherwise masked by energetically dominant post-breakup structures in full-field decompositions. Three dominant structure classes are identified: global liquid-column flapping, pre-breakup surface waves on the windward column surface, and periodic post-breakup structures including bags, ligaments, and droplet clusters.
2. Surface-wave wavelength decreases and frequency increases monotonically with We_g in the column and early bag-breakup regimes, consistent with shorter instability wavelengths selected under stronger aerodynamic shear. Post-breakup structure wavelength reaches a local minimum near the bag-to-multimode transition. Both structure types share propagation speeds close to the liquid-jet velocity within the bag-breakup regime, while post-breakup structure propagation speed progressively exceeds the jet velocity in the multimode and shear breakup regimes.
3. Pre-breakup surface waves are consistent with a convective Kelvin–Helmholtz mechanism. Measured surface-wave wavelengths agree with theoretical most-unstable wavelengths from the classical two-layer KH dispersion relation in both magnitude and trend, and measured propagation speeds close to the liquid-jet velocity confirm that wave selection is governed by gas-liquid interfacial shear while downstream propagation is controlled by liquid-column convection.
4. A hierarchical nesting relationship exists between surface waves and post-breakup structures within the bag-breakup regime. Near-constant wavelength ratios, frequency

ratios, and near-unity propagation speed ratios within each liquid-jet velocity group indicate that breakup structures emerge as nonlinear secondary structures periodically selected from a precursor KH wave train, rather than as independently driven dynamical processes.

5. The four breakup regimes reflect the competition between KH-driven interfacial-wave growth and direct aerodynamic stripping. KH waves are present but sub-threshold in the column regime; periodic breakup structures coexist with surface waves in the bag regime; both mechanisms operate simultaneously in the multimode regime; and stripping dominates in the shear regime, suppressing organised bag formation entirely.

These results demonstrate that POD-based modal analysis provides an effective and systematic framework for quantifying multi-scale LJIC atomisation dynamics, linking experimentally observable interfacial structures to their underlying instability mechanisms across a wide range of operating conditions.

Reference

Arienti, M., & Soteriou, M. C. (2009). Time-resolved proper orthogonal decomposition of liquid jet dynamics. *Physics of Fluids*, *21*(11), 112104. https://doi.org/10.1063/1.3263165

Berkooz, G., Holmes, P., & Lumley, J. L. (1993). The Proper Orthogonal Decomposition in the Analysis of Turbulent Flows. *Annual Review of Fluid Mechanics*, *25*(Volume 25, 1993), 539–575. https://doi.org/10.1146/annurev.fl.25.010193.002543

Bhatia, B., Johny, T., & De, A. (2023). Understanding the liquid jet break-up in various regimes at elevated pressure using a compressible VOF-LPT coupled framework. *International Journal of Multiphase Flow*, *159*, 104303. https://doi.org/10.1016/j.ijmultiphaseflow.2022.104303

Chandrasekhar, S. (1981). *Hydrodynamic and Hydromagnetic Stability*. Courier Corporation.

Charalampous, G., Hadjiyiannis, C., & Hardalupas, Y. (2016). Comparative measurement of the breakup length of liquid jets in airblast atomisers using optical connectivity, electrical connectivity and shadowgraphy. *Measurement*, *89*, 288–299. https://doi.org/10.1016/j.measurement.2016.03.062

Charalampous, G., Hadjiyiannis, C., & Hardalupas, Y. (2019). Proper orthogonal decomposition of primary breakup and spray in co-axial airblast atomizers. *Physics of Fluids*, *31*(4), 043304. https://doi.org/10.1063/1.5085416

Drazin, P. G., & Reid, W. H. (2004). *Hydrodynamic Stability* (2nd edn). Cambridge University Press. https://doi.org/10.1017/CBO9780511616938

Harikumar, H., Vincent Raj, A., & Sadanandan, R. (2025). Characterization of liquid jet breakup mechanisms in a swirl coaxial aerated injector. *Experiments in Fluids*, *67*(1), 2. https://doi.org/10.1007/s00348-025-04154-2

Johnson, J. A., Marsh, A. W., Douglas, E. J., Ochs, B. A., Hammack, S. D., Menon, S., & Mazumdar, Y. C. (2024). Digital holography for the study of non-aerated liquid jets in supersonic crossflow. *Proceedings of the Combustion Institute*, *40*(1), 105471. https://doi.org/10.1016/j.proci.2024.105471

Leask, S. B., & McDonell, V. G. (2019). *On the Physical Interpretation of Proper Orthogonal Decomposition and Dynamic Mode Decomposition for Liquid Injection* (arXiv:1909.07576). arXiv. https://doi.org/10.48550/arXiv.1909.07576

Lefebvre, A. H., & McDonell, V. G. (2017). *Atomization and Sprays* (2nd edn). CRC Press. https://doi.org/10.1201/9781315120911

Lin, S. P. (2003). *Breakup of Liquid Sheets and Jets*. Cambridge University Press. https://doi.org/10.1017/CBO9780511547096

Lumley, J. L. (1967). *The structure of inhomogeneous turbulent flows*. 166–178. https://scispace.com/papers/the-structure-of-inhomogeneous-turbulent-flows-3efejj2ujg

Mahesh, K. (2013). The Interaction of Jets with Crossflow. *Annual Review of Fluid Mechanics*, *45*(Volume 45, 2013), 379–407. https://doi.org/10.1146/annurev-fluid-120710-101115

Medipati, C., Govardhan, R. N., Deivandran, S., & Tropea, C. (2025). Elliptic liquid jets in a supersonic cross-flow. *Journal of Fluid Mechanics*, *1014*, A34. https://doi.org/10.1017/jfm.2025.10317

Michalke, A. (1964). On the inviscid instability of the hyperbolictangent velocity profile. *Journal of Fluid Mechanics*, *19*(4), 543–556. https://doi.org/10.1017/S0022112064000908

Ng, C.-L., Sankarakrishnan, R., & Sallam, K. A. (2008). Bag breakup of nonturbulent liquid jets in crossflow. *International Journal of Multiphase Flow*, *34*(3), 241–259. https://doi.org/10.1016/j.ijmultiphaseflow.2007.07.005

Sallam, K. A., Aalburg, C., & Faeth, G. M. (2004). Breakup of Round Nonturbulent Liquid Jets in Gaseous Crossflow. *AIAA Journal*, *42*(12), 2529–2540. https://doi.org/10.2514/1.3749

Sallam, K. A., Dai, Z., & Faeth, G. M. (2002). Liquid breakup at the surface of turbulent round liquid jets in still gases. *International Journal of Multiphase Flow*, *28*(3), 427–449. https://doi.org/10.1016/S0301-9322(01)00067-2

Shaw, V. G., Elliott, P., Boller, M., & Gutmark, E. J. (2024). The breakup and instability structures of liquid jets in subsonic crossflows. *Experimental Thermal and Fluid Science*, *155*, 111176. https://doi.org/10.1016/j.expthermflusci.2024.111176

Sirovich, L. (1987). Turbulence and the dynamics of coherent structures. I. Coherent structures. *Quarterly of Applied Mathematics*, *45*, 561–571. https://doi.org/10.1090/qam/910462

Soni, S. K., & Kolhe, P. S. (2021). Liquid jet breakup and spray formation with annular swirl air. *International Journal of Multiphase Flow*, *134*, 103474. https://doi.org/10.1016/j.ijmultiphaseflow.2020.103474

Wang, T., & Hardalupas, Y. (2023). Combined optical connectivity and optical flow velocimetry measurement of interfacial velocity of a liquid jet in gas crossflow. *International Journal of Multiphase Flow*, *168*, 104581. https://doi.org/10.1016/j.ijmultiphaseflow.2023.104581

Wang, T., & Hardalupas, Y. (2025). The physics of primary breakup of a liquid jet in crossflow: A study based on interfacial characteristics. *International Journal of Multiphase Flow*, *193*, 105397. https://doi.org/10.1016/j.ijmultiphaseflow.2025.105397

Welch, P. (1967). The use of fast Fourier transform for the estimation of power spectra: A method based on time averaging over short, modified periodograms. *IEEE Transactions on Audio and Electroacoustics*, *15*(2), 70–73. https://doi.org/10.1109/TAU.1967.1161901

Wu, P.-K., Kirkendall, K. A., Fuller, R. P., & Nejad, A. S. (1997). Breakup Processes of Liquid Jets in Subsonic Crossflows. *Journal of Propulsion and Power*, *13*(1), 64–73. https://doi.org/10.2514/2.5151

Zhou, D., Chang, J., Tang, C., & He, L. (2023). Review on research progress in liquid jet in crossflow. *International Communications in Heat and Mass Transfer*, *148*, 107003. https://doi.org/10.1016/j.icheatmasstransfer.2023.107003